



Effects of geometry and composition of soft polymer films embedded with nanoparticles on rates for optothermal heat dissipation

Journal:	<i>Nanoscale</i>
Manuscript ID	NR-ART-02-2018-000977.R1
Article Type:	Paper
Date Submitted by the Author:	04-Apr-2018
Complete List of Authors:	Roper, Donald; University of Arkansas, Chemical Engineering Berry, Keith; University of Arkansas, Chemical Engineering Dunklin, Jeremy; National Renewable Energy Laboratory, Chemistry & Nanoscience Center Chambers, Caitlyn; University of Arkansas, Ralph E. Martin Department of Chemical Engineering Bejugam, Vinith; university of arkansas, Chemical Engineering Forcherio, Gregory; US Army Research Laboratory, Sensors & Electron Devices Directorate Lanier, Megan; University of Arkansas, Chemical Engineering

Effects of geometry and composition of soft polymer films embedded with nanoparticles on rates for optothermal heat dissipation

*D. Keith Roper,^{1, 2, 3} * Keith R. Berry Jr.,¹ Jeremy R. Dunklin,^{1, 4} Caitlyn Chambers,¹ Vinith Bejugam,¹ Gregory T. Forcherio,^{2, 5} and Megan Lanier¹*

¹ Ralph E. Martin Department of Chemical Engineering, University of Arkansas, Fayetteville, AR 72701, USA

² Microelectronics-Photonics Graduate Program, University of Arkansas, Fayetteville, AR 72701, USA

³ Institute for Nanoscience and Engineering, University of Arkansas, Fayetteville, AR 72701, USA

⁴ Chemistry & Nanoscience Center, National Renewable Energy Lab, Golden, CO, 80401 USA

⁵ Sensors & Electron Devices Directorate, U.S. Army Research Laboratory, Adelphi, MD, 20783 USA

* Corresponding Author

ABSTRACT

Embedding soft matter with nanoparticles (NPs) can provide electromagnetic tunability at sub-micron scales for growing number of uses in healthcare, sustainable energy, and chemical processing. But use of NP-embedded soft material in temperature-sensitive applications has been constrained by difficulty in validating prediction of rates for energy dissipation across thermally insulating to conducting behavior. This work improved embedment of monodisperse NP to stably decrease inter-NP spacings in polydimethylsiloxane (PDMS) to nano-scales. Lumped-parameter and finite element analyses were refined to apportion effects of structure and composition of NP-embedded soft polymer to rates for conductive, convective, and radiative heat dissipation. These advances allowed rational selection of PDMS size and NP composition to optimize measured rates of internal (conductive) and external (convective and radiative) heat dissipation. Stably reducing distance between monodisperse NP to nano-scale intervals increased overall heat dissipation rate by up to 29%. Refined fabrication of NP-embedded polymer enabled tunability of dynamic thermal response, the ratio of internal to external dissipation rate, by a factor of 3.1 to achieve a value of 0.091, the largest reported to date. Heat dissipation rates simulated *a priori* were consistent with 130 μm resolution thermal images across 2- to 15-fold changes in NP-PDMS geometry and composition. Nusselt number was observed to increase with the fourth root of Rayleigh number across thermally insulative and conductive regimes, further validating the approach. These developments support model-informed design of soft media embedded with nano-scale spaced NP to optimize heat dissipation rates for evolving temperature-sensitive diagnostic and therapeutic modalities as well as emerging uses in flexible bioelectronics, cell and tissue culture, and solar-thermal heating.

1. INTRODUCTION

Electromagnetically-active nanoparticles (NP) embedded in soft matter exhibit enhanced thermal properties¹⁻⁷ and efficiencies^{8,9} that augment energy and mass transport in numerous systems.^{10,11}

Soft abiotic material containing nanoparticles has been shown to induce hyperthermia in photothermal¹² and chemo-thermal¹³ therapy, photosensitization to inactivate bacteria,^{14–16} targeted drug release,^{17,18} contrast in medical images,¹⁹ and gene transfection.¹² In particular, resonant laser irradiation of NP in soft polymers results in characteristic dissipation of thermal energy as heat.^{20–22} Functional descriptions of heat dissipated from pulsed or continuous resonant excitation²³ are relevant for use in designing and optimizing cancer ablation,^{24–27} catalytic reaction,²⁸ membrane separation,²⁹ microfluidic flux,³⁰ and photothermal therapy.^{31–38}

Rigorous comparison, however, of simulated data with measured energy output by irradiated NP has largely considered heat dissipated at thermal equilibrium as a function of NP size/shape/composition in one of two scenarios: (i) monodisperse NP(s) suspended in fluid, deposited or formed on ceramic or semiconductor, or diluted into soft material such that neighboring NP are microns or more apart; or (ii) polydisperse NP reduced by biological or chemical means into soft material to achieve high NP density. As a result, NP-transduced heating in soft matter like gels and tissues for temperature sensitive applications e.g., clinical diagnostic and therapy, remains limited by lack of data for non-equilibrium (transient) rates of heat dissipation¹⁸ which are critical to biological outcomes^{39,40}; scant evaluation of heating from monodisperse NP embedded in soft matter below micron-scale spacing; and scarcity⁴¹ and difficulties^{42,43} comparing simulation with experimental data to evaluate effects of soft matter size, shape, density, thermal conductivity or NP concentration on transient heat dissipation at nano- to micron scales.

Landau damping of localized surface plasmons induced by resonant irradiation of NP dissipates energy via charge-transfer and/or heating of surrounding media via conduction, convection and radiation.⁴⁴ To date, simulation of phase change,^{45,46} ultrafast dynamics,^{47–49} and light-to-heat conversion^{8,50–54} in nanocomposites has characterized primarily steady-state components of energy flux, e.g., radiative heat transfer,^{44,55–58} phonon transport,⁵⁹ thermal conductivity,^{60–62} and Brownian dynamics^{61,63,64} or total energy dissipation.^{23,50,65} Yet predictability of even steady-state temperature in homogeneous media embedded with evenly-dispersed, uniformly-sized NP remains challenging.^{54,66} For example, increasing NP concentration was recently reported to paradoxically result in tumor regrowth⁴² despite increased temperatures due to reduced depth of laser penetration.⁶⁷ Such anomalies due to optothermal aspects that differ from conventional bulk, radiant, or resistive modes call for rigorous comparison of measured optothermal heat dissipation with conventional conductive, convective and radiative mechanisms.

The transient (dynamic) rate of temperature increase, i.e., heating rate, is a critical factor influencing a variety of biomedical outcomes. A heat rate not less than 1°C per minute has been advised for superficial hyperthermia clinical trials.³⁹ The heating rate of NP-containing material was reported to vary nearly 3-fold depending on the configuration of NPs.⁶⁸ Heating transients can influence rate of drug release from polydimethylsiloxane (PDMS) films⁴⁰ and phase change materials.^{69–72} Biocompatibility, optical transparency, and thermal properties support use of NP-embedded soft polymer like PDMS in targeted drug release,⁴⁰ photoacoustic imaging,¹⁹ gene transfection and photothermal therapy.¹² PDMS is widely used as a tissue phantom, i.e., surrogate, to characterize spectral and thermal features of tissue⁷³ in hyperthermia,³⁹ photodynamic therapy, and optical coherence tomography.

Heat dissipated at steady-state by plasmon resonant NP dispersed into various polymer films of micro- to nano-scale thickness was recently observed to scale with the amount of incident optical power extinguished.^{74,75} This was demonstrated by finite element simulation of heat dissipation that integrated relations for Fourier conduction, Rayleigh convection and Stefan-Boltzmann radiation to conservation of energy in the film.⁵⁰ Steady-state, micro-scale profiles of dissipated heat were dependent on micro- versus nano-scale film thickness and super- versus sub-wavelength inter-NP separation. Interestingly, both Maxwell Garnett effective medium theory and coupled dipole approximation showed temperature increase per NP ultimately diminished at high loadings. The reported consistency between measured heat dissipation and corresponding simulated values at steady state indicates finite element analysis could also distinguish effects of geometry of soft matter and embedded NP size/shape/composition on transient rates for heat dissipation via internal (conduction) and external (convection and radiation) processes.

The present work examined changes in the transient rate for heat dissipation as inter-NP separation was reduced from greater than 5 microns to sub-micron intervals while varying the 3D geometry of a polymer and its NP density 2- to 15-fold. It validated use of a compact structure-function relation for *a priori* design and optimization of thin PDMS films embedded with increasing number of monodisperse gold (Au) NPs to transition the films from thermally insulating to conducting behavior. Rates for heat dissipation estimated *a priori* using both the analytic structure-function relation and finite element simulation were consistent with measured values across significant parameter variations: film thicknesses from 0.7 to 1.5 mm, Au content from 0.001 (2.34×10^{11} NP cm⁻³) to 0.015 mass % (35.2×10^{11} NP cm⁻³), two forms of AuNPs (monodisperse spheres vs. randomly reduced polydisperse NP), and two sizes of monodisperse AuNPs: 16 nm (non-scattering) and 76 nm (scattering and absorbing). Rates for buoyant heat convection were observed to depend on the fourth root of the Rayleigh number, validating the structure-function relations across thermally insulating to thermally conducting behavior. A refined fabrication approach allowed NP-to-NP spacings to be reduced to nano-scale values approaching the resonant wavelength. Such proximity enhanced apparent Nusselt number, i.e., the ratio of convective to conductive heat transfer, by up to 29% and increased dynamic thermal responses by 3.1-fold to achieve the largest reported value for dynamic thermal response to date. Together these advances support rational design and optimization of NP-embedded soft material with high dynamic thermal responses for use in diagnostics, therapeutics, and sustainable energy, particularly in heat-sensitive circumstances.

2. MATERIALS AND METHODS

2.1 Film Fabrication and AuNP Addition. A previously reported method⁶⁵ to fabricate AuNP-PDMS films was refined to increase NP content while eliminating observable gas/vapor entrapment and NP aggregation. The refined method increased AuNP content 15-fold up to a mass percent in PDMS of 0.015% while at the same time decreasing inter-NP spacing to the nano-scale without detectable aggregation. Briefly, dried, poly(vinylpyrrolidone) (PVP)-coated AuNPs (Nanocomposix Inc., San Diego, CA) were dispersed into isopropanol (IPA) to 1 mg mL⁻¹. Monodisperse AuNPs of 16 nm and 76 nm mean diameter (see supporting information (SI) for size distribution and absorption spectra) were dispersed into PDMS (Sylgard® 184 silicone elastomer kit #4019862, Dow Corning, Midland, MI) at 10^{11} - 10^{12} and 10^{10} NP cm⁻³, respectively, using the following approach. PDMS monomer and crosslinker were mixed at a 10:1 ratio and

degassed for 2 hours. A volume of AuNP-IPA dispersion selected to achieve a targeted AuNP density was added into uncured PDMS and mixed while degassing for 1 hour. A 1.5 g mass of AuNP-IPA-PDMS was poured into a 25 mm x 25 mm x 1 mm polystyrene sample box and cured at 60 °C for 24 hours. The box was wrapped in foil to prevent light-induced curing. Compared to the previous method, the method reported in this work extended the degas time of the polymer and cross linker; optically isolated curing samples; reduced the cure temperature; and extended the cure time. These changes minimized observable gas/vapor bubble formation and entrapment as well as polymer defects and NP conglomerates, which improved the overall structure and performance of the nanocomposite films. These refinements enabled AuNP content to be increased 150-fold to 0.015% by mass in soft matter while simultaneously decreasing inter-NP spacing to nano-scales for the first time without detectable aggregation. Figure 1 shows frontal and cross-section images of ca. 5 mm x 5 mm films containing (a) 16 nm (above) and (b) 76 nm (below) nm spherical AuNP. From left to right in each row, film color changed from dark red to slightly pink as Au content decreased. Length and width of films varied across a range of $28 \leq L \times W \leq 35 \text{ mm}^2$ enabling analysis of dissipation rate sensitivity to film geometry. Corresponding values of measured thickness, Au content (in both NP per cm^3 and mass percent) and average NP-to-NP separation distance as measured by the Wigner Seitz radius are shown below each film.

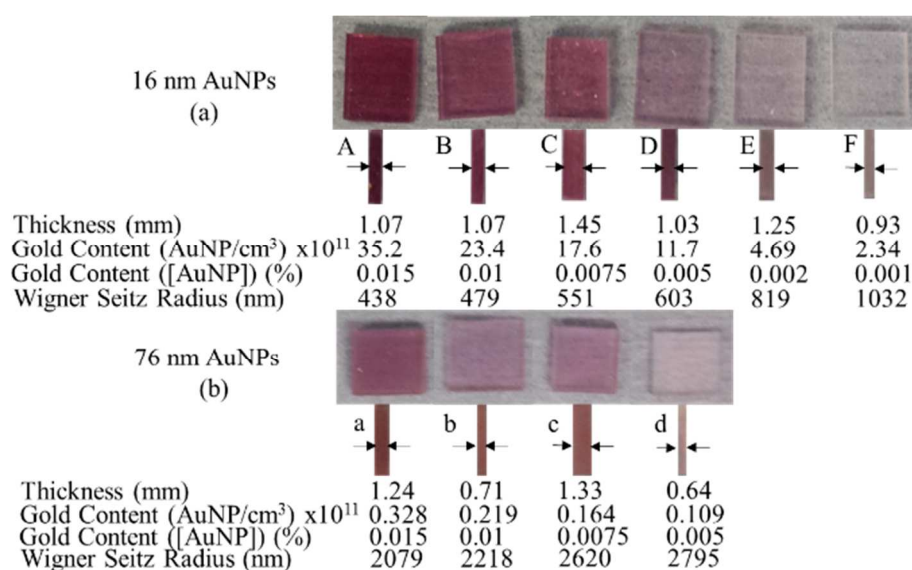


Figure 1. Optical images of ca. 5 x 5 mm PDMS films (above facing; below side) containing monodisperse 16 nm (a; above) and 76 nm (b; below) AuNPs. AuNP content decreases from left to right in (a) and (b) as given in the text below each film. Images of films containing polydisperse, reduced AuNP (rAuNP), categorized as Film II in Table, are shown in SI.

2.2 Au Content Calculations. The total mass of monodisperse AuNPs in PDMS was determined by multiplying the volume of AuNP-containing stock solution added to the PDMS by (i) the concentration of stock solution, (ii) the volume of a single AuNP, $(4\pi r_p/3)^3$ where r_p is AuNP radius, and (iii) Au density, $\rho_{\text{Au}}=19.3 \text{ g/cm}^3$. The mass percent of AuNPs in PDMS was calculated by dividing the mass of added AuNPs by the mass of solution (PDMS mass plus AuNP mass) and multiplying by 100%. Wigner-Seitz radius, r_{W-S} , was calculated as $r_{W-S} = r_p(\rho_{\text{Au}}/x)^{1/3} = (3V/4\pi N)^{1/3}$, where x is Au mass per cubic centimeter of host media, V is media volume, and N is the number of AuNPs added to volume V . Twice the value of r_{W-S} reduced by

twice the value of r_p is an estimate of NP-to-NP separation distance for randomly-dispersed AuNP at a particular concentration.

2.3 Thermal Characterization. AuNPs embedded in PDMS films fabricated using the refined method herein were irradiated resonantly using a 532 nm laser (MXL-FN-532, CNI, Changchun, China) at 25 or 100 mW. Laser power was recorded using a power meter (PM310D, Thorlabs, Newton, NJ). Incident laser power during the 3-minute heating period was measured to be within $\pm 1.05\%$ at 25 and 100 mW. This was well within the laser manufacturer's specification of ± 1 to 10%. The power meter was rated for a calibration uncertainty of $\pm 3.3\%$ at 1064 nm and $\pm 5\%$ at 190 nm – 1064 μm . Infrared images of the AuNP-PDMS nanocomposites were captured at 5 images per second over 6 minutes (min): 0:10 min ambient conditions, 2:50 min laser irradiation, and 3:00 min cooling using an infrared thermal imaging camera (ICI 7320, Infrared Cameras Inc., Beaumont, TX). A laser shutter (SH05, Thorlabs, Newton, NJ) and shutter controller (SC10, Thorlabs, Newton, NJ) were used to open and close laser at each time interval (see SI for schematic of thermal setup). A K-type thermocouple recorded ambient temperature ~ 1 cm away from the nanocomposite to compare with IR camera ambient readings. Each AuNP-PDMS film was mounted with tweezers to position the incident laser spot at the film top center. All power incident on the Film I samples was contained with a laser spot with $D4\sigma$ diameter of 3 mm. The thermal measurement apparatus was isolated from ambient light and forced convection by enclosure in an opaque chamber. Two or more replicates were measured. Temperature values reported are from one representative cooling period.

2.4 Measured Total Dissipation Rates. Measured total time for heat dissipation, τ_T^{-1} , during cooling was determined using temperature data extracted from the raw thermal images using MATLAB R2015b (Mathworks, Natick, MA). The MATLAB code divided the images into pixelated temperature heat maps. Maximum (ambient) temperature at each pixel was evaluated by averaging measured temperature equilibrated at laser-heated (ambient) conditions over the final 30 s of laser heating (final 5 seconds of cooling). Values of maximum temperature, T_{max} , and ambient temperature, T_{amb} , at each pixel were used to calculate a dimensionless temperature driving force, $\theta = (T_{\text{amb}} - T)/(T_{\text{amb}} - T_{\text{max}})$, at every pixel, where T was the measured time-varying temperature during cooling after laser irradiation. Plotting the natural log of the driving force vs. time for a 45 s cooling period for the 16 and 76 nm films and 30 s cooling period for the rAuNP films yielded τ_T^{-1} at each pixel. The value of τ_T^{-1} was the negative inverse of the linearly regressed slope. This process of measuring τ_T^{-1} is illustrated in Figure 2(b). In calculating θ , values of temperature below T_{amb} were excised to eliminate imaginary results when calculating τ_T^{-1} . Mean values of T_{max} , T_{amb} , T , and τ_T^{-1} across the film face were determined by averaging pixelated values for maximum, ambient, and transient temperatures and thermal dissipation times, respectively.

2.5 Predicted Total Dissipation Rates.

2.5.1 Compact Structure Function Relation. Summing a series of consecutive thermal resistances, R_i , yields the overall thermal resistance, $R_T = \sum_i R_i$. Here subscript i identifies components with distinguishable thermal resistances, i.e., internal vs. external thermal dissipation rates. Rewriting this sum in terms of dissipation rates, with time constants being proportional to resistances yields²³

$$\frac{1}{\tau_T} = \frac{1}{\sum_i \tau_i} = \frac{1}{\tau_{int} + \tau_{ext}} \quad (1)$$

where τ_{int} and τ_{ext} are the internal and external time constants for thermal dissipation respectively. Decomposing each time constant into independently measurable, composition-dependent thermodynamic and geometric parameters²³ shows the total thermal dissipation rate of a plasmonic system is a function of its external dissipation, τ_{ext} , relative to its intrinsic internal dissipation, τ_{int} , viz.,

$$\tau_{ext} = \sum_i \frac{m_i C_{p,i}}{U} = \frac{kLWD}{\alpha U} \quad (2a)$$

$$\tau_{int} = \frac{L_c^2}{\alpha} \quad (2b)$$

where, m_i is mass, $C_{p,i}$ is heat capacity, k is thermal conductivity, L , W , and D are sample length, width and thickness, respectively, L_c is a characteristic thermal length of the sample ($D/2$ for thin films in current work), α is the mass-averaged thermal diffusivity calculated on a percent mass basis, and U is an overall heat transfer coefficient⁴⁵ given by

$$U \equiv \frac{k_c A_c}{L_{c,e}} + h_{conv} A_s + A_s \varepsilon \sigma (T^2 + T_{amb}^2) (T + T_{amb}) \quad (3)$$

where k_c is the thermal conductivity of the heat-conductive material, A_c is the contact area perpendicular to conduction, $L_{c,e}$ is a characteristic length for conduction to the environment, h_{conv} is the heat transfer coefficient for convection, A_s is the surface area of the film, ε is the emissivity of the material, σ is the Stefan-Boltzmann constant, and T_{amb} is the ambient temperature. The value of T used in Equation 3 was the average surface temperature at hot equilibrium, T_{max} .

Films were oriented vertically to allow laser irradiation and temperature mapping from opposite sides. Therefore, h_{conv} was estimated using²³

$$h_{conv} = \frac{k}{L_c} [0.59 Ra_L^{1/4}] \quad (4)$$

where k is thermal conductivity and L_c is defined as the height of the plate in the vertical direction. The Rayleigh number is $Ra_L = g \rho^2 \beta C_p (T - T_{amb}) L^3 / k \mu$ where g is acceleration due to gravity, β is the coefficient of thermal expansion of air, ρ is the density of air, C_p is the heat capacity of air, k is the thermal conductivity of air, and μ is the viscosity of air. L for this system was equivalent to L_c in Equation 4.

To analyze Nusselt number, Nu , dependence, estimated values of h_{conv} were determined using Equation 4. Measured values of h_{conv} were calculated from observed data as follows. Measured τ_{int} and τ_T values were used to calculate τ_{ext} using Equations 1-2. From this value of τ_{ext} , a measured value of U was obtained from Equation 3 using $\tau_{ext} = kLWD/\alpha U$. Thermal conductivity of air made the conduction term in Equation 3 negligible. The radiation term was calculated using measured parameters. Then h_{conv} was obtained from Equation 2 and used in $Nu = h_{conv} L_c / k$ where h_{conv} , L_c , and k were as defined in Equation 4.

2.5.2 Finite Element Analysis. Finite element heat transfer analysis (FEA) was conducted using the Heat Transfer in Solids module in version 5.2a of COMSOL Multiphysics (Stockholm, Sweden) as described previously.⁵⁰ Briefly, concurrent internal and external heat dissipation in AuNP-PDMS films was modeled using Fourier's law for conductive heat transfer and the convective heat transfer coefficient for a vertical plate defined in Equation 4 coupled with radiation as defined in Equation 3 rightmost term. For the current work, temperature profiles of each film at the instant the laser irradiation ceased were imported into COMSOL. An initial 2D conjugate model using Heat Transfer in Solids and Gaussian Cooling (via Rayleigh convection and Stefan-Boltzmann radiation) was applied to the model to estimate the cooling curve for each film. Temperature changes at each second over a 45 s period were computed using a COMSOL Dynamic Study function. A 'cut plane' was then used to extract the temperature across the entire surface of the film at each second. These values were imported into MATLAB where an average value for τ_T^{-1} was calculated using the approach described in §2.4 *Measured Total Dissipation Rates*.




3. RESULTS AND DISCUSSION

This study evaluated transient (dynamic) rates of temperature change due to spectrothermal heat dissipation in soft PDMS embedded with dispersed, uniformly-sized AuNP or electrochemically-reduced, heterogeneously-sized AuNP down to inter-NP spacing of nano-scales for the first time. The biocompatibility, optical transparency, and thermal properties of NP-PDMS nanocomposites support their use in targeted drug release,⁴⁰ photoacoustic imaging,¹⁹ gene transfection and photothermal therapy,¹² and tissue phantoms.⁷³ Beyond use in these evolving therapeutic and diagnostic modalities, PDMS is employed in emerging biomedical technologies that leverage activity of nano-scale matter. PDMS factors into synthetic extracellular matrix (ECM) to form a facile, biocompatible substrate for cell and tissue culture^{76,77} whose properties may be enhanced by incorporation of nano-scale materials, e.g., graphene. PDMS is key to fabricating flexible, stretchable electronics.⁷⁸⁻⁸¹

Thermal dissipation by resonantly-induced NP in soft matter differs from energy dissipation in such media when they are heated by conventional bulk or resistive means. In conventionally-heated media, micro- to macro-scale bulk, surface, or linear thermal sources drive heat flux from an interface into an adjacent target media in a direction opposite to a developing temperature gradient.⁸² In contrast, irradiation of optically-active NP embedded in soft media originates heat at point sources within the media. NP irradiation can augment energy dissipation relative to surface or linear sources. For example, resonant induction of plasmonic near fields on NP may induce NP re-radiation as well as absorptive thermal dissipation.⁸³ Wavelength-scale inclusions (e.g., voids) and/or surface reflection may induce concurrent geometric scattering.^{9,84} Such re-radiated, scattered, and reflected incident photons supplement point-source plasmon heating, thereby changing thermal response, heat flux, and equilibrium temperature relative to values predicted or observed when such optical or plasmonic effects are absent.⁵⁰ This potential augmentation relative to conventional conductive, convective and radiative energy flux due to bulk, surface or linear thermal sources requires quantitative consideration as well as experimental validation in order to accurately describe magnitudes and parametric variation of steady-state and transient energy dissipation in soft material embedded with spectrothermal NP.

Soft polymer films embedded with two types of NP that were examined herein are characterized in Table 1. AuNP-PDMS films labeled ‘Film I’ were fabricated by a refined process to increase the content of monodisperse (i.e., uniformly-sized) Au nanospheres thereby reducing inter-NP spacing to the nano-scale and to vary film thickness while eliminating observable entrapment of gas or vapor and AuNP aggregation. AuNP-PDMS films labeled ‘Film II’ were fabricated by electrochemical reduction of Au into polydisperse (i.e., heterogeneously-sized) NP with varying morphology (size/shape). Samples of Film I exhibited higher equilibrium temperature increase per power input ($\Delta T/\text{watt}$) and Au content and lower inter-NP spacing than such films fabricated previously. The present work compared a greater range of film dimensions and AuNP sizes side-by-side than had been previously characterized. The films exhibited (i) $\Delta T/\text{watt}$ increasing 3.2-fold, from 93.8 °C per watt (Film 6: polydisperse rAuNP at 0.0141 mass %) to 304 °C per watt (Film A: monodisperse AuNP at 0.015 mass %); and (ii) Film I thickness ranging up to 2.1-fold, from 0.64 mm to 1.45 mm. Film II thicknesses were constant at 0.68 mm.

Table 1. Characteristics of PDMS thin films embedded with two different types of nanoparticles.

	Film I ⁶⁵	Film II ¹
Description	Monodisperse Au nanospheres in PDMS	Polydisperse reduced AuNP (rAuNP) in PDMS ^a
Dimensions LxWxD (mm)	$28 \leq L \times W \leq 35 \text{ mm}^2$ $0.64 \leq D \leq 1.45 \text{ mm}$	5.0 x 5.0 x 0.68
AuNP type	 16 nm PVP coated AuNP ^b  76 nm PVP coated AuNP ^c	 rAuNP reduced from H ₂ AuCl ₄
Gold content (mass %)	16 nm: 0.001 to 0.015 76 nm: 0.005 to 0.015	0.007 to 0.190
Measured overall thermal equilibration time, τ_T (s)	16 nm: 40.4 to 53.3 76 nm: 29.1 to 57.9	15.9 to 27.1
ΔT_{eq} (K)	16 nm: 1.3 to 7.6 76 nm: 2.0 to 5.2	5.4 to 34.9
Laser wavelength (nm)	532	532
Laser power (mW)	25	100
Laser spot size (mm)	3	≤ 2
Irradiation time (s)	180	180

^a PDMS dielectric constant = 2.02 . PDMS refractive index = 1.42

^b Diameter = $15.4 \pm 2.4 \text{ nm}$ (mean \pm one standard deviation). Coefficient of variation = 15.3%

^c Diameter = $76 \pm 13 \text{ nm}$ (mean \pm one standard deviation). Coefficient of variation = 16.5%

Only geometric (L, W, and D) and compositional (mass%) properties of NP-embedded soft films in Table 1 and relevant material properties (k , C_p , and ρ) were used in the compact relations in Equations 1 to 3 to estimate corresponding rates of heat dissipation. In section 3.1, these analytic *a priori* estimates were compared in Fig. 2(c) with FEA simulated heat dissipation and with values measured for soft PDMS films embedded with two forms of AuNPs. The broad range of parameter values shown in Table 1, enabled by refined AuNP-PDMS film fabrication herein, supported characterization of heat dissipation rates in insulative (thicker and/or less NP) and conductive (thinner and/or more NP) films. Use of Equations 1-3 across this entire range was validated by an increase in Nusselt number with the fourth root of Rayleigh number observed in

Figure 3. Section 3.2 examined relative contributions to the overall rate of heat dissipation from internal and external processes. Specific application to rate-dependent cancer photothermal therapy and sustainable energy processes were evaluated. External dissipation via convection into adjacent fluid and radiation into the surroundings largely determined the overall rate of energy flow. Interestingly, decreasing inter-NP separation distances down to nano-scales enhanced the overall rate by as much as 29% relative to estimates. However, non-negligible internal dissipation via conduction in the solid phase decreased the overall energy dissipation rate, as insulation by the soft polymer film increased with thickness and with lesser NP content. This is illustrated in Figure 4. In section 3.3, geometry and inter-NP separation of soft polymer films guided by Equations 1-3 were shown to yield soft matter with a large range (Figure 5) of thermal dynamics and transient rates for heat dissipation. Improved AuNP-PDMS fabrication herein allowed decreasing inter-NP separation to achieve the highest dynamic thermal response measured to date. Tunability of thermal response is particularly important in temperature-sensitive applications.

3.1 Total Heat Dissipation Rates of Metal-Polymer Thin Films. For refined Film I, values of total dissipation rate, τ_T^{-1} , estimated *a priori* using either Equations 1-3 or finite element analysis were within 24% of experimentally measured rates across significant changes in diameter (5-fold) and concentration (15-fold) of uniform AuNP embedded into PDMS films of varying thickness (2-fold). Measured values of τ_T^{-1} were determined⁴⁴ as the negative inverse of the slope from a linear regression of the natural log of the temperature driving force, $\theta = (T_{\text{amb}} - T)/(T_{\text{amb}} - T_{\text{max}})$ vs. time, as detailed in §2.4 *Measured Total Dissipation Rates*. Figure 2(a) shows a map of equilibrium temperature at the onset of the cooling period. Figure 2(b) illustrates a plot of natural log of the temperature driving force, $\ln \theta$, versus time used to determine a measured value of τ_T . Estimated values of τ_T^{-1} were determined *a priori* from independently measured physical characteristics of each film by using Equations 1-3. FEA of τ_T^{-1} was done using COMSOL and MATLAB, as detailed in §2.5 *Predicted Total Dissipation Rates*.

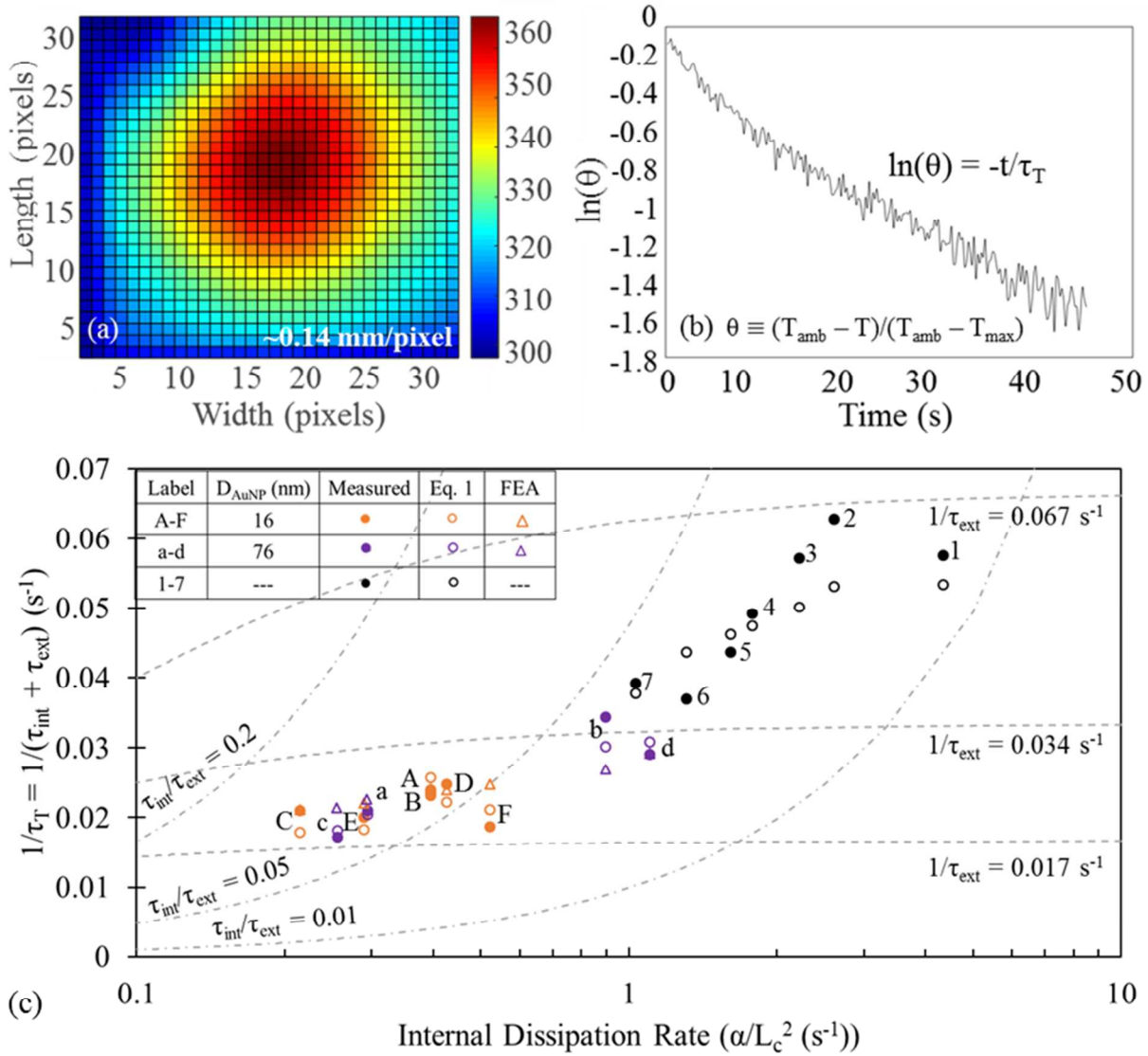


Figure 2. (a) Temperature map of film 1 (0.1896 % rAuNP-PDMS). (b) A single pixel representative plot of the measured $\ln(\theta)$ vs time from film F used to calculate measured value of τ_T . (c) Total dissipation rate, τ_T^{-1} , values obtained from measurement (closed circles), *a priori* estimates using Equations 1 to 3 (open circles), and FEA simulation (open triangles) for AuNP-PDMS films containing 16 nm (orange symbols), 76 nm (purple symbols), and *in situ* reduced (black symbols) AuNP. Dashed and dash-dot lines show constant values of external dissipation rate, τ_{ext}^{-1} , and thermal dynamic ratio, $\tau_{\text{int}}/\tau_{\text{ext}}$, respectively.

The refined fabrication method expanded the ranges of attainable Au content, inter-NP spacing, film thickness, and equilibrium temperature per power input ($\Delta T/\text{watt}$). This resulted in AuNP-PDMS films with widely tunable external and internal thermal dynamics that spanned thermally conductive and thermally insulative behavior. As shown in Figure 2(c), the characteristic time for heat dissipation via radiation, convection and conduction from a film to its environment, τ_{ext} , varied 4.5-fold across the films examined from a low near 13.0 s ($\tau_{\text{ext}}^{-1} = 0.077 \text{ s}^{-1}$; measured Film 1; closed circle near top of Figure 2(c)) to a high of 57.7 s ($\tau_{\text{ext}}^{-1} = 0.017 \text{ s}^{-1}$; measured Film

c; closed circle near bottom of Figure 2(c)). At the same time, the characteristic time required for internal temperature equilibration due to conduction within the film, τ_{int} , relative to time required for external dissipation (i.e., τ_{int}/τ_{ext}) ranged 5.8 fold from negligible ($\tau_{int}/\tau_{ext} = 0.017$; measured Film 1; closed circle on RHS of Figure 2(c)) to non-negligible ($\tau_{int}/\tau_{ext} = 0.098$; Film C; closed circle on LHS of Figure 2(c)).

Overall, the magnitudes of *a priori* estimates of τ_T^{-1} calculated with Equations 1 to 3 remained consistent with both measured and FEA-simulated values across significant variations in internal (τ_{int} , 20.2-fold), external, (τ_{ext} , 4.5-fold) and overall (τ_{int}/τ_{ext} , 5.8-fold) thermal dynamics. Figure 2(c) compares values of τ_T^{-1} that were measured (closed circles), calculated *a priori* with Equations 1 to 3 (open circles), and simulated by FEA (open triangles) for 16 nm (orange), 76 nm (purple) and reduced (black) AuNPs. Lines with dashes and dash-dots indicate constant values of external dissipation rate, τ_{ext}^{-1} , and overall thermal dynamic ratio, τ_{int}/τ_{ext} , respectively. The dash-dot line for constant $\tau_{int}/\tau_{ext} \sim 0.05$ divides Figure 2(c) into two regimes: an insulative regime as τ_{int}/τ_{ext} increases to 0.1 or greater and a conductive regime as τ_{int}/τ_{ext} decreases to 0.01 or less. In the insulative regime, the rate for internal heat dissipation via conduction becomes significant relative to external heat dissipation, which occurs primarily via convection and radiation. This lowers the overall rate for NP-induced optothermal heat dissipation relative to τ_{ext}^{-1} . The internal dissipation rate, dominated by geometric (characteristic film thickness, L_c) and compositional (thermal diffusivity, α) parameters, reduces the overall rate. In the conductive regime, the overall rate for optothermal heat dissipation approaches the rate for external heat dissipation. The relative effect of internal dissipation diminishes. Significantly, for $\tau_{int}/\tau_{ext} \geq 0.01$ both internal and external rates for heat dissipation must be considered to accurately characterize the overall rate for optothermal dissipation.

The Rayleigh number (Ra) dependence of convective heat transfer coefficients obtained from measured heat dissipation rates was evaluated to validate use of Equations 1 to 3 to describe AuNP-PDMS films. The Nusselt number (Nu) has a $1/4$ power dependence on the Ra.⁸² This dependence is indicated by the dash-dot line in Figure 3. Ra is the product of Grashoff (Gr) and Prandtl (Pr) numbers. Heat transfer coefficients obtained from measured heat dissipation rates (filled symbols) distributed normally around theoretically expected values for both 16 (orange) and 76 nm (purple) AuNP as well as for reduced AuNP (black symbols, inset). Nu, Ra, and heat transfer coefficient were calculated as described in §2.5.1 *Compact Structure Function Relation*.

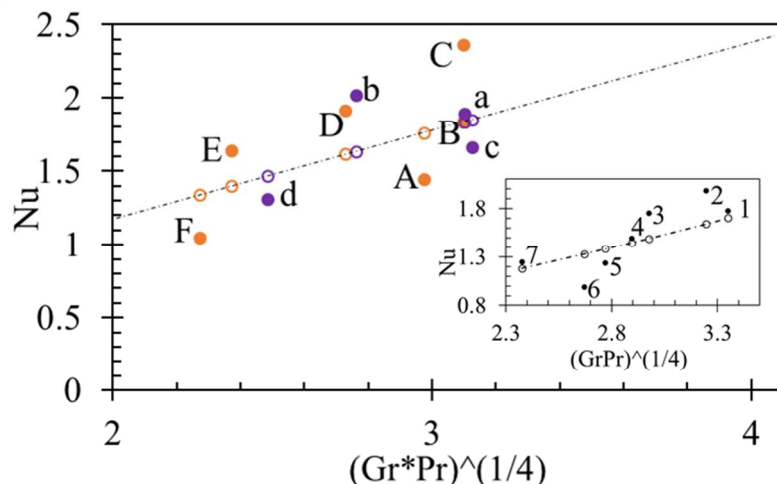


Figure 3. Measured (filled symbols) versus estimated (open symbols) Nu calculated using Equation 4, plotted vs. $GrPr^{1/4}$ for monodisperse 16 nm (orange), 76 nm (purple), and polydisperse reduced AuNPs (inset, black). Normal variation of measured data around the mean supports utility of Equations 1 to 3 for characterizing overall rates for optothermal heat dissipation.

3.2 Tunable Total Dissipation and Dynamic Thermal Response. The compact structure-function relations in Equations 1 to 3 directly apportion variations in composition and geometry of the AuNP-polymer films to changes in internal and external dissipation rates as shown in Figures 2(c) and 3. This provides insights that are valuable for applications ranging from sustainable energy to human health.

Overall, Figure 2(c) and Equation 1 show that decreases in overall heat dissipation rate occur nonlinearly and with increasing magnitude as the rate of internal temperature equilibration due to conduction within the film approaches the rate of external heat dissipation due to heat transfer with the surroundings. Such decreases are most prominent for films with higher external heat transfer rates, e.g., for $\tau_{ext}^{-1} = 0.077$ as opposed to $\tau_{ext}^{-1} = 0.017$. For example, a value of $\tau_{int}/\tau_{ext} = 0.1$ yields a 10% decrease in overall heat dissipation as a result of slow conduction with the film.

The utility of the intuitive understanding of relative effects of internal and external dissipation rates provided by Equations 1 to 3 is illustrated by considering a recent reported on nanocomposites in sustainable energy. Kosuga *et al.* reported that heat dissipation lowered the temperature induced after 100 s of artificial AM 1.5G (i.e., 1 sun) incidence on ca. 0.2 mm transparent polyethylene naphthalate (PEN) films. Measured temperatures for films embedded with fixed beads (FBs) decorated with Au and silver (Ag) NP decreased from 120 °C (expected) to 43.4 °C (measured) and 40 °C (expected) to 36.8 °C (measured), respectively.⁵² From the cooling curves reported for PEN films embedded with AuNP-FBs and AgNP-FBs, we calculated corresponding total thermal dissipation rates by the method in §2.4 *Measured Total Dissipation Rates* to be 0.036 and 0.031 s^{-1} , respectively. Interestingly, these overall rates for thermal dissipation were similar to those of Films b, 6 and 7 (all ca. 0.7 mm thick; see Figure 2(c)), although the PEN films were 29% as thick. Setting $L_c = 0.1$ mm and using the bulk thermal diffusivity of PEN film, internal dissipation rate could be estimated to be 5.88 s^{-1} . This internal dissipation rate was higher than values from Film 2 on the RHS of Figure 2(c). Relative to the

high NP-FB-film internal dissipation rate, the external dissipation rate for the PEN films was thus <1%. The structure-function relations in Equations 1 to 3 illustrated by Figure 2(c) identify three specific possible approaches to increase the induced temperature of a PEN film so that it approaches a higher expected value: (i) decrease internal dissipation rate (i.e., increase L_c or reduce α); (ii) decrease external convection (i.e., reduce h_{conv}); and/or (iii) decrease external radiation (e.g., reduce emissivity, ϵ).

Across the data for all films in Figure 2(c), the overall rate for heat dissipation was increased 3.6-fold from 0.017 to 0.063 s^{-1} by varying the diameter (5-fold) and concentration (15-fold) of uniform AuNP embedded into PDMS films of varying thickness (2-fold). The corresponding compact, *a priori* description of total heat dissipation rate allows design of NP-induced thermalization. This has broad utility, as illustrated by considering results from Tang *et al.* who showed Au nanorods (NRs) coated with a shell of platinum (Pt) nanodots (Au@Pt) were more efficient photothermal therapy (PTT) agents than bare AuNRs, killing >80 % of cancer cells vs. <50 %, respectively, both *in vitro* and *in vivo*.²⁴ From cooling curves and physical properties reported for Au@Pt and AuNRs, measured total thermal dissipation rates were calculated as in §2.4 *Measured Total Dissipation Rates* to be 0.0031 and 0.0025 s^{-1} , respectively, for coated and bare AuNR. These rates are ~7-fold lower than values measured herein for nanocomposite films. These rates are comparable to values reported previously for aqueous Au nanosphere suspensions, estimated using the compact description (Equations 1 to 3 in §2.5.1 *Compact Structure Function Relations*).²³ Correspondence between rates for heat dissipation from tissue-embedded and aqueous-suspended AuNPs appears attributable to the primarily aqueous content of cells. Notably, overall rates for heat dissipation appeared slightly lower for the less efficient AuNR PTT agents, i.e., bare AuNRs. That greater heat dissipation rate improved PTT efficiency is consistent with clinical assessment of superficial hyperthermia which advises a heat rate not less than 1°C per minute for clinical trials.³⁹ It indicates that a geometry- or composition-dependent influence on dynamic thermal dissipation rate that is detrimental to PTT could be mitigated using alterations guided by the structure-function relations of Equations 1 to 3.

Comparing estimates from Equations 1 to 3 with measurements in Figure 2(c) identifies opportunities to further enhance optothermal transduction. For example, measured values of external dissipation rate for AuNP-PDMS films with higher AuNP content for both 16 and 76 nm particles exceeded estimates, with the exception of film A. Thermal dissipation from films with more concentrated AuNP and/or larger NP appeared more likely to be enhanced by resonant optical reflection or scattering.⁶⁵ Such effects are not accounted in the compact description for dynamic thermal response in Equations 1 to 3. As a second example, total heat dissipation rate for PDMS films into which AuNP had been reduced *in situ* (black symbols) varied primarily with Au content. Au content in these films increased from 0.007% to nearly 0.2% (from left to right in Figure 2(c)); the geometry of these films was kept constant. In contrast, total dissipation rates for 16 nm (orange symbols) and 76 nm (purple symbols) varied with both geometry and Au content. Exchanging the global value of T_{max} for its local pixelated value did not appreciably change measured or estimated total dissipation rates.

Accounting for internal (τ_{int}^{-1}) as well as external (τ_{ext}^{-1}) contributions to heat dissipation improves *a priori* description of the overall rate for heat dissipation (τ_T^{-1}). Figure 4 compares estimated rates for total heat dissipation (filled circles; left y-axis) and external heat dissipation

(open triangles; right y-axis) from 16 nm (orange) or 76 nm (purple) AuNP embedded in PDMS films with corresponding measured values (x-axis). Across the range of heat dissipation rates measured for the films (0.017 to 0.035 s⁻¹), estimates for most films (A,B,F,a,c,and d) were nearer measured values when τ_{int}^{-1} as well τ_{ext}^{-1} were used to calculate τ_T^{-1} via Equation 1. As examples, estimated τ_T^{-1} for Films a and B (filled circles) shown near the dot-dash line in Figure 4 were within 2.6 and 1.4 % of measured values, respectively. Adding internal (τ_{int}^{-1}) contributions to heat transfer lowered the estimated value of τ_T^{-1} relative to its measured counterpart in films for which apparent Nu exceeded its *a priori* estimate by Equation 4, as shown in Figure 3. In these films (C,D,E, and b), resistance to internal dissipation appeared negligible and the estimate for τ_{ext}^{-1} in Equation 2(a) agreed better with τ_T^{-1} measured from the overall sample. Notably, Film E had measured and estimated dissipation rates near that of Film a despite a 14.2-fold higher AuNP concentration (4.7x10¹¹ NP cm⁻³ in E vs 0.33 x10¹¹ in a) and a 4.8-fold smaller AuNP size (16 nm for E vs. 76 nm for a) resulting in a 7.5-fold lower mass percent Au (0.002% in E vs. 0.015% in a). Measured thicknesses for Films E and a were 1.25 and 1.24 mm, respectively. This underscored primary control of dissipation rate by film thickness at relatively low gold content (i.e., the insulative regime).

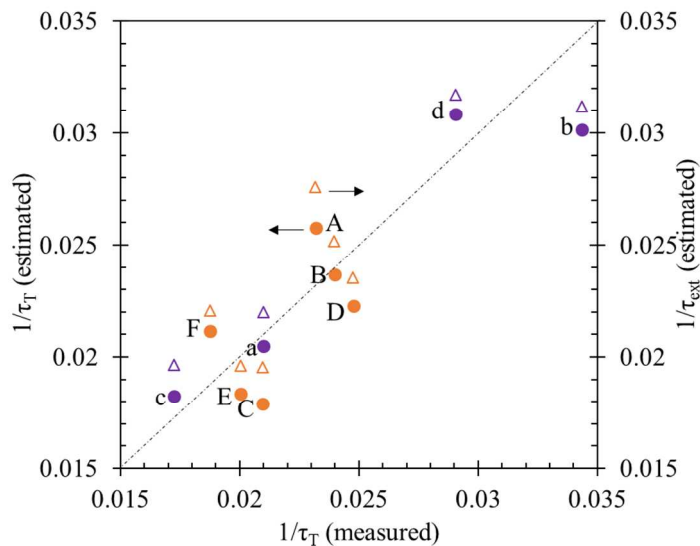


Figure 4. Estimated rates for total heat dissipation (filled circles; left y-axis) and external heat dissipation (open triangles; right y-axis) compared with corresponding measured values (x-axis). Results shown are for thin PMDS films embedded with 16 nm (orange) or 76 nm (purple) spherical AuNP.

3.3 Thermal Dynamics of Metal-Polymer Thin Films. The rate at which thermal energy was dissipated from a system to its environment relative to the rate of internal thermal equilibrium was characterized by the ratio τ_{int}/τ_{ext} , termed the dynamic thermal response. Higher dynamic thermal responses are indicative of highly insulative films for which internal dissipation rate must be accounted to accurately estimate the overall rate for heat dissipation *a priori*. Lower dynamic thermal responses are indicative of more conductive films. There the external dissipation dominates and internal dissipation becomes negligible in Equation 1. In Figure 5, effects on dynamic thermal response of geometry and composition for nanocomposite thin films evaluated in this work are examined by taking the ratio of Equation 2(b) to 2(a) using parameters

identified in Figure 2.1 and described in §2.5 *Predicted Total Dissipation Rates*. Figure 5 distinguishes the two thermal response regimes identified in Figure 2(c): an insulative regime as τ_{int}/τ_{ext} approaches 0.1 where internal dissipation rates less than about 1 s^{-1} result in the overall rate for optothermal dissipation rate being lowered as film thickness increases; and a conductive regime as τ_{int}/τ_{ext} approaches 0.01 where internal dissipation rates greater than about 1 s^{-1} result in the overall rate for energy dissipation being increased by a larger Au content.

For larger insulating films, Au content was increased to $\leq 0.015\%$ ($35.2 \times 10^{11} \text{ NP cm}^{-3}$) to achieve nano-scale inter-NP separations. Film geometry exhibited a predominant influence on τ_{int}/τ_{ext} . Samples from Film I and Film II groups had thicknesses that increased 2.1-fold and area cross sections that increased 1.1-fold. This yielded an overall increase in dynamic thermal response by a factor of 3.1 ($0.091/0.029$), the largest reported to date. The structure-function relation in Equation 1 more accurately predicted rates for heat dissipation from such insulating films than previous methods. This occurred because modest increases in sample thickness in insulative films rapidly raised internal dissipation times to values that were non-negligible relative to external equilibration times due to the stochastic nature of temperature dissipation. In other words, insulating films with non-negligible internal dissipation rates are ‘thermally thick’. For example, increasing the thickness from 1.0 to 1.5 mm yielded a 2-fold increase in internal dissipation and a >1.5 fold increase in dynamic thermal response. Decreasing the thickness from 1.3 to 0.7 mm resulted in a 4-fold decrease in internal dissipation and a >1.5 -fold decrease in dynamic thermal response.

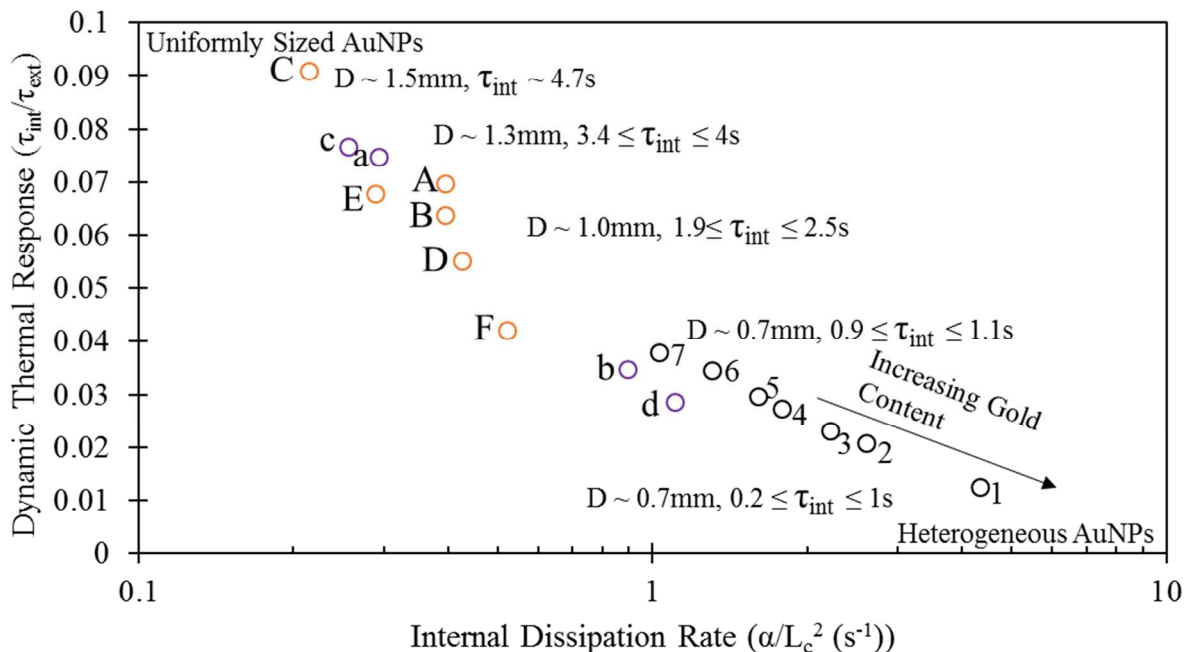


Figure 5. Dynamic thermal response increases as internal dissipation rate decreases for films with 16 nm (A-F, open orange circles), 76 nm (a-d, open purple circles), and heterogeneous (open black circles) AuNP. All labels start at highest AuNP concentration and go toward lowest AuNP concentration.

In contrast, thinner films into which Au was reduced exhibited a 3-fold decrease in dynamic thermal response as Au content increased 27-fold from 0.007 to 0.19 mass %. The time for internal thermal equilibration was lower than characteristic time for external heat dissipation in these films resulting in ‘thermally thin’ behavior. Thus the thermal response was determined primarily by Au content, rather than film thickness. This difference occurred despite compositional similarities with the thicker films. These results were consistent with previous reports for AuNP reduced onto conductive SiO₂ substrates that exhibited negligible internal dissipation rates, $\tau_{int} \ll \tau_{ext}$, and corresponding low dynamic thermal responses.²³ Note that values for NP cm⁻³ could not be determined for AuNP-reduced films because particle size and size distribution of reduced NPs was not known.⁹ Also, accounting for temperature dependence of PDMS geometric and thermodynamic parameters resulted in less than 2.5% differences in values calculated for dynamic thermal response.

Importantly, *a priori* estimates of rates for optothermal heat dissipation in Figures 2 through 5 were obtained with Equations 1 to 3 using only geometric (L, W, and D) and thermodynamic (k, C_p, and ρ) parameters for material with embedded nanoparticles at ambient conditions. Figure 2 shows good correspondence between *a priori* estimates calculated analytically or simulated by FEA and values measured for soft PDMS films embedded with two forms of AuNPs across a broad range of parameter values. Figure 3 shows the compact structure function relations in Equations 1 to 3 provide consistency with fundamental description of convective, conductive and radiative heat transfer. Figure 4 illustrates the importance of considering both internal and external dissipation rate in evaluating overall rate for heat dissipation in a AuNP-polymer nanocomposite. Embedding NP – particularly small, non-scattering nanoparticles - in soft matter at concentrations that yield nanometer-scale separation distances was likelier to exhibit transient rates of heat dissipation that exceed estimated values after accounting for internal conduction as well as and external conduction, convection and radiation. Figure 5 identifies a large range of thermal dynamics and transient rates for heat dissipation possible in similar nanocomposite films as a result of variations in geometry and composition. This range spanned insulative and conductive regimes, in which trends in dynamic thermal response arose primarily due to film thickness and AuNP content in thermally thick and thin films, respectively. The compact structure function relations in Equations 1 to 3 thus provide a facile tool by which changes in the transient overall rate for heat dissipation from optothermal NP can be quickly, directly and scalably attributed to specific parameter(s). These relations and the refined fabrication method exhibit usefulness in specifying the geometry and composition of NP-embedded films that demonstrably impact rates for heat dissipation in photothermal energy, tissue ablation, membrane separation, or catalytic reaction.

4. CONCLUSIONS

Effects of geometry and composition on the transient rate for optothermal dissipation from resonantly irradiated NP were examined in soft PDMS thin films using compact structure function relations and finite element analysis. A refined fabrication method that stably reduced inter-NP distance to nano-scale intervals increased energy dissipation by up to 29%. For both 16 and 76 nm diameter AuNP embedded in PDMS at 0.015 mass % (35.2×10^{11} NP cm⁻³) or less, film thickness controlled dynamic thermal response and total dissipation rate when non-negligible internal dissipation rates approached 10% of external dissipation rates, i.e., the

insulative regime. Increasing film thickness from 0.7 to 1.5 mm reduced total measured dissipation rate from 0.063 to 0.017 s⁻¹ and increased dynamic thermal response from 0.029 to 0.091. The latter value was the highest increased dynamic thermal response observed to date. Measured total dissipation rates across the entire film were within 24% of estimates from the compact description across a range of sample thicknesses from 0.64 to 1.45 mm, Au content from 0.001 (2.34 x 10¹¹ NP cm⁻³) to 0.015 mass % (35.2 x 10¹¹ NP cm⁻³) for 16 nm and 0.005 (0.109 x 10¹¹ NP cm⁻³) to 0.015 mass % (0.328 x 10¹¹ NP cm⁻³) for 76 nm, and area from 28 to 35 mm². Good correspondence between *a priori* estimates by the compact structure function relation or finite element analysis and measures from refined AuNP-PDMS films across an expanded range of geometric and thermodynamic parameters demonstrates important progress toward rational design and development of optothermal nanocomposites with tunable dynamic thermal responses.

AUTHOR INFORMATION

Corresponding author

* E-mail: dkroper@uark.edu, phone: (801) 891-8921.

Author Contributions

D. K. Roper derived the approach, directed the work, analyzed data, refined figures, and prepared, revised and finalized the text. K. R. Berry Jr. performed numerical analysis, prepared and refined figures and drafted text. J. R. Dunklin fabricated films and performed initial calculations. C. Chambers performed the thermographic experiments of the 16 and 76 nm films and initial data analysis. V. Bejugam performed COMSOL simulations for cooling dissipation rates. G. T. Forcherio provided guidance for experiments and calculations. M. Lanier showed mass-averaged thermal parameter values for lower AuNP contents were not needed using volume fraction calculations from Maxwell relationships in Ref.⁸²

ACKNOWLEDGMENTS.

This work was supported in part by NSF CBET-1134222, NSF ECCS-1006927, the University of Arkansas Foundation, and the Walton Family Charitable Foundation. J.R. Dunklin and G.T. Forcherio acknowledge support from respective NSF GRFP awards. Any opinions, findings, and conclusions or recommendations expressed in this material are those of the authors and do not necessarily reflect the views of the National Science Foundation.

CONFLICTS OF INTEREST.

There are no conflicts of interest to declare.

REFERENCES.

1. Berry, K. R., Russell, A. G., Blake, P. T. & Roper, D. K. Gold nanoparticles reduced in situ and dispersed in polymer thin films: optical and thermal properties. *Nanotechnology*

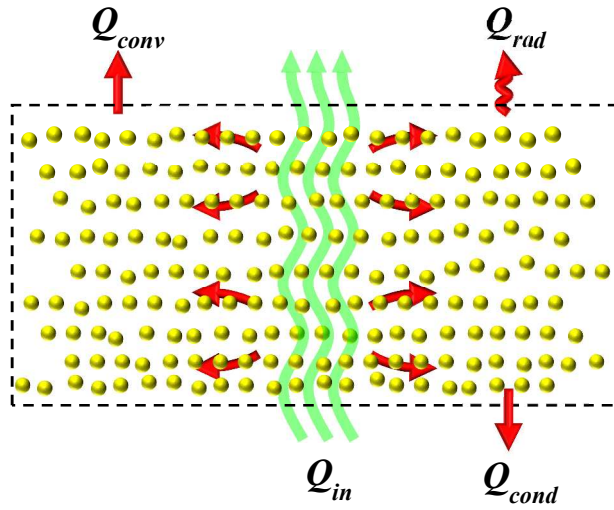
- 23**, 11 (2012).
2. Bozlar, M. *et al.* Carbon nanotube microarchitectures for enhanced thermal conduction at ultralow mass fraction in polymer composites. *Adv. Mater.* **22**, 1654–1658 (2010).
 3. Dunklin, J. R., Forcherio, G. T., Berry, K. R. & Roper, D. K. Asymmetric Reduction of Gold Nanoparticles into Thermoplasmonic Polydimethylsiloxane Thin Films. *ACS Appl. Mater. Interfaces* **5**, 8457–8466 (2013).
 4. Li, T.-L. & Hsu, S. L.-C. Enhanced thermal conductivity of polyimide films via a hybrid of micro- and nano-sized boron nitride. *J. Phys. Chem. B* **114**, 6825–6829 (2010).
 5. Lin, W., Moon, K. S. & Wong, C. P. A combined process of in situ functionalization and microwave treatment to achieve ultrasmall thermal expansion of aligned carbon nanotube-polymer nanocomposites: Toward applications as thermal interface materials. *Adv. Mater.* **21**, 2421–2424 (2009).
 6. Urban, A. S. *et al.* Optical trapping and manipulation of plasmonic nanoparticles: fundamentals, applications, and perspectives. *Nanoscale* **6**, 4458 (2014).
 7. Chen, M. *et al.* Plasmonic Nanoparticle-Embedded Poly(p-phenylene benzobisoxazole) Nanofibrous Composite Films for Solar Steam Generation. *Nanoscale* **10**, 6186–6193 (2018).
 8. Ahn, W. & Roper, D. K. Transformed gold island film improves light-to-heat transduction of nanoparticles on silica capillaries. *J. Phys. Chem. C* **112**, 12214–12218 (2008).
 9. Forcherio, G. T. & Roper, D. K. Optical attenuation of plasmonic nanocomposites within photonic devices. *Appl. Opt.* **53**, 6417–6427 (2013).
 10. Cho, E. S. *et al.* Engineering Synergy: Energy and Mass Transport in Hybrid Nanomaterials. *Adv. Mater.* **27**, 5744–5752 (2015).
 11. Volokitin, A. I. & Persson, B. N. J. Radiative heat transfer between nanostructures. *Phys. Rev. B* **63**, 205404 (2001).
 12. Byeon, J. H. & Kim, Y.-W. Gas-phase self-assembly of soft nanocomposites for efficient gene transfection and photothermal therapy. *J. Mater. Chem. B* **2**, 3185 (2014).
 13. Byeon, J. H. Aerosol Nanoencapsulation: Single-Pass Floating Self-Assembly of Biofunctional Hybrid Nanoplatfoms. *ACS Appl. Mater. Interfaces* **8**, 17757–17762 (2016).
 14. Noimark, S., Dunnill, C. W. & Parkin, I. P. Shining light on materials — A self-sterilising revolution. *Adv. Drug Deliv. Rev.* **65**, 570–580 (2013).
 15. Bovis, M. J. *et al.* Photosensitisation studies of silicone polymer doped with methylene blue and nanogold for antimicrobial applications. *RSC Adv.* **5**, 54830–54842 (2015).
 16. Sehmi, S. K. *et al.* Enhancing the Antibacterial Activity of Light-Activated Surfaces Containing Crystal Violet and ZnO Nanoparticles: Investigation of Nanoparticle Size, Capping Ligand, and Dopants. *ACS Omega* **1**, 334–343 (2016).
 17. Alexandra S. Angelatos, Benno Radt, and & Caruso*, F. Light-Responsive Polyelectrolyte/Gold Nanoparticle Microcapsules. *J. Phys. Chem. B* **109**, 3071–3076 (2005).
 18. Kaur, P., Aliru, M. L., Chadha, A. S., Asea, A. & Krishnan, S. Hyperthermia using nanoparticles--Promises and pitfalls. *Int. J. Hyperth.* **32**, 76–88 (2016).
 19. Shi, Y., Qin, H., Yang, S. & Xing, D. Thermally confined shell coating amplifies the photoacoustic conversion efficiency of nanoprobles. *Nano Res.* **9**, 3644–3655 (2016).
 20. Rashidi-Huyeh, M. & Palpant, B. Thermal response of nanocomposite materials under pulsed laser excitation. *J. Appl. Phys.* **96**, 4475–4482 (2004).

21. Worajittiphon, P., Jurewicz, I., King, A. A. K., Keddie, J. L. & Dalton, A. B. Enhanced Thermal Actuation in Thin Polymer Films Through Particle Nano-Squeezing by Carbon Nanotube Belts. *Adv. Mater.* **22**, 5310–5314 (2010).
22. Zimovets, S. V. & Geshev, P. I. Nonstationary heating of two-dimensional metal nanoparticles by laser radiation. *J. Eng. Phys. Thermophys.* **81**, 976–984 (2008).
23. Berry, K. R., Dunklin, J. R., Blake, P. A. & Roper, D. K. Thermal dynamics of plasmonic nanoparticle composites. *J. Phys. Chem. C* **119**, 10550–10557 (2015).
24. Tang, J. *et al.* Au@Pt nanostructures: a novel photothermal conversion agent for cancer therapy. *Nanoscale* **6**, 3670 (2014).
25. Xu, Y. *et al.* Progress in materials for thermal ablation of cancer cells. *J. Mater. Chem.* **22**, 20128 (2012).
26. Zhang, J. Z. Biomedical applications of shape-controlled plasmonic nanostructures: A case study of hollow gold nanospheres for photothermal ablation therapy of cancer. *J. Phys. Chem. Lett.* **1**, 686–695 (2010).
27. Zhang, H. *et al.* A multi-functional nanoplatform for tumor synergistic phototherapy. *Nanotechnology* **27**, 65104 (2016).
28. Wang, C. *et al.* Visible light plasmonic heating of Au–ZnO for the catalytic reduction of CO₂. *Nanoscale* **5**, 6968 (2013).
29. Vanherck, K., Hermans, S., Verbiest, T. & Vankelecom, I. Using the photothermal effect to improve membrane separations via localized heating. *J. Mater. Chem.* **21**, 6079 (2011).
30. Li, Y., Verbiest, T. & Vankelecom, I. Improving the flux of PDMS membranes via localized heating through incorporation of gold nanoparticles. *J. Memb. Sci.* **428**, 63–69 (2013).
31. Jaque, D. *et al.* Nanoparticles for photothermal therapies. *Nanoscale* **6**, 9494–9530 (2014).
32. Qin, J. *et al.* Gold nanorods as a theranostic platform for in vitro and in vivo imaging and photothermal therapy of inflammatory macrophages. *Nanoscale* **7**, 13991–14001 (2015).
33. Zhou, J. *et al.* Hybridized doxorubicin-Au nanospheres exhibit enhanced near-infrared surface plasmon absorption for photothermal therapy applications. *Nanoscale* **7**, 5869–5883 (2015).
34. Clemenson, S., David, L. & Espuche, E. Structure and Morphology of Nanocomposite Films Prepared from Polyvinyl Alcohol and Silver Nitrate: Influence of Thermal Treatment. *J. Polym. Sci. Part A Polym. Chem.* **45**, 2657–2672 (2007).
35. Lisunova, M. *et al.* Photothermal response of the plasmonic nanoconglomerates in films assembled by electroless plating. *RSC Adv.* **4**, (2014).
36. Lisunova, M., Dunklin, J. R., Jenkins, S. V., Chen, J. & Roper, D. K. The unusual visible photothermal response of free standing multilayered films based on plasmonic bimetallic nanocages. *RSC Adv.* **5**, 15719–15727 (2015).
37. Pustovalov, V., Astafyeva, L. & Jean, B. Computer modeling of the optical properties and heating of spherical gold and silica-gold nanoparticles for laser combined imaging and photothermal treatment. *Nanotechnology* **20**, 225105 (2009).
38. Ricciardi, L. *et al.* Plasmonic mediated cancer phototherapy: the combined effect of thermal and photodynamic processes. *Nanoscale* **9**, 19279–19289 (2017).
39. Dobšíček Trefná, H. *et al.* Quality assurance guidelines for superficial hyperthermia clinical trials. *Strahlentherapie und Onkol.* **193**, 351–366 (2017).
40. Scott, A., Gupta, R. & Kulkarni, G. U. A Simple Water-Based Synthesis of Au Nanoparticle/PDMS Composites for Water Purification and Targeted Drug Release.

- Macromol. Chem. Phys.* **211**, 1640–1647 (2010).
41. Kannadorai, R. K. & Liu, Q. Optimization in interstitial plasmonic photothermal therapy for treatment planning. *Med. Phys.* **40**, 103301 (2013).
 42. Jang, B., Kim, Y. S. & Choi, Y. Effects of Gold Nanorod Concentration on the Depth-Related Temperature Increase During Hyperthermic Ablation. *Small* **7**, 265–270 (2011).
 43. Ruta, S., Chantrell, R. & Hovorka, O. Unified model of hyperthermia via hysteresis heating in systems of interacting magnetic nanoparticles. *Sci. Rep.* **5**, 9090 (2015).
 44. Roper, D. K., Ahn, W. & Hoepfner, M. Microscale Heat Transfer Transduced by Surface Plasmon Resonant Gold Nanoparticles. *J. Phys. Chem. C* **111**, 3636–3641 (2007).
 45. Russell, A. G., McKnight, M. D., Sharp, A. C., Hestekin, J. A. & Roper, D. K. Gold Nanoparticles Allow Optoplasmonic Evaporation from Open Silica Cells with a Logarithmic Approach to Steady-State Thermal Profiles. *J. Phys. Chem. C* **114**, 10132–10139 (2010).
 46. Russell, A. G., McKnight, M. D., Hestekin, J. A. & Roper, D. K. Thermodynamics of Optoplasmonic Heating in Fluid-Filled Gold-Nanoparticle-Plated Capillaries. *Langmuir* **27**, 7799–7805 (2011).
 47. Chen, J., Walther, J. H. & Koumoutsakos, P. Ultrafast cooling by covalently bonded graphene-carbon nanotube hybrid immersed in water. *Nanotechnology* **27**, 465705 (2016).
 48. Maity, S. *et al.* Spatial temperature mapping within polymer nanocomposites undergoing ultrafast photothermal heating via gold nanorods. *Nanoscale* **6**, 15236–15247 (2014).
 49. Melinger, J. S. *et al.* Ultrafast dynamics of gold-based nanocomposite materials. *J. Phys. Chem. A* **107**, 3424–3431 (2003).
 50. Dunklin, J. R., Forcherio, G. T., Berry, K. R. & Roper, D. K. Gold nanoparticle-polydimethylsiloxane thin films enhance thermoplasmonic dissipation by internal reflection. *J. Phys. Chem. C* **118**, 7523–7531 (2014).
 51. Fu, G., Sanjay, S. T., Dou, M. & Li, X. Nanoparticle-mediated photothermal effect enables a new method for quantitative biochemical analysis using a thermometer. *Nanoscale* **8**, 5422–5427 (2016).
 52. Kosuga, A., Yamamoto, Y., Miyai, M. & Matsuzawa, M. Electronic Supplementary Information A high performance photothermal film with spherical shell-type metallic nanocomposites for solar thermoelectric conversion. *Nanoscale* **7**, 1–2 (2015).
 53. Mishra, N. K., Kumar, V. & Joshi, K. B. Thermoplasmonic effect of silver nanoparticles modulates peptide amphiphile fiber into nanowreath-like assembly. *Nanoscale* **7**, 20238–20248 (2015).
 54. Richardson, H. H., Carlson, M. T., Tandler, P. J., Hernandez, P. & Govorov, A. O. Experimental and theoretical studies of light-to-heat conversion and collective heating effects in metal nanoparticle solutions. *Nano Lett.* **9**, 1139–1146 (2009).
 55. Ekici, O. *et al.* Thermal analysis of gold nanorods heated with femtosecond laser pulses. *J. Phys. D. Appl. Phys.* **41**, 185501 (2008).
 56. Sassaroli, E., Li, K. C. P. & O'Neill, B. E. Numerical investigation of heating of a gold nanoparticle and the surrounding microenvironment by nanosecond laser pulses for nanomedicine applications. *Phys. Med. Biol.* **54**, 5541–5560 (2009).
 57. Smith, B. E., Roder, P. B., Zhou, X. & Pauzauskie, P. J. Nanoscale materials for hyperthermal theranostics. *Nanoscale* **7**, 7115–7126 (2015).
 58. Zhou, N., Traverso, L. M. & Xu, X. Power delivery and self-heating in nanoscale near field transducer for heat-assisted magnetic recording. *Nanotechnology* **26**, 134001 (2015).

59. Jeng, M.-S., Yang, R., Song, D. & Chen, G. Modeling the Thermal Conductivity and Phonon Transport in Nanoparticle Composites Using Monte Carlo Simulation. *J. Heat Transfer* **130**, 42410 (2008).
60. Yang, R. & Chen, G. Thermal conductivity modeling of periodic two-dimensional nanocomposites. *Phys. Rev. B - Condens. Matter Mater. Phys.* **69**, 1–10 (2004).
61. Almusallam, A. S. & Sholl, D. S. Brownian dynamics study of polymer-stabilized nanoparticles. *Nanotechnology* **16**, S409-15 (2005).
62. Baral, S., Rafiei Miandashti, A. & Richardson, H. H. Near-field thermal imaging of optically excited gold nanostructures: scaling principles for collective heating with heat dissipation into the surrounding medium. *Nanoscale* **10**, 941–948 (2018).
63. Millen, J., Deesuwana, T., Barker, P. & Anders, J. Nanoscale temperature measurements using non-equilibrium Brownian dynamics of a levitated nanosphere. *Nat. Nanotechnol.* **9**, 425–429 (2013).
64. Gardea, F., Glaz, B., Riddick, J., Lagoudas, D. C. & Naraghi, M. Identification of energy dissipation mechanisms in CNT-reinforced nanocomposites. *Nanotechnology* **27**, 105707 (2016).
65. Dunklin, J. R., Forcherio, G. T. & Keith Roper, D. Gold nanoparticle-polydimethylsiloxane films reflect light internally by optical diffraction and Mie scattering. *Mater. Res. Express* **2**, 85005 (2015).
66. Qin, Z. *et al.* Quantitative Comparison of Photothermal Heat Generation between Gold Nanospheres and Nanorods. *Sci. Rep.* **6**, 29836 (2016).
67. Vera, J. & Bayazitoglu, Y. A note on laser penetration in nanoshell deposited tissue. *Int. J. Heat Mass Transf.* **52**, 3402–3406 (2009).
68. Santos, G. M. *et al.* Photothermal inactivation of heat-resistant bacteria on nanoporous gold disk arrays. *Opt. Mater. Express* **6**, 256863 (2016).
69. Li, W. *et al.* Gold nanocages covered with thermally-responsive polymers for controlled release by high-intensity focused ultrasound. *Nanoscale* **3**, 1724–30 (2011).
70. Moon, G. D. *et al.* A New Theranostic System Based on Gold Nanocages and Phase-Change Materials with Unique Features for Photoacoustic Imaging and Controlled Release. *J. Am. Chem. Soc.* **133**, 4762–4765 (2011).
71. Sun, T. *et al.* Using SV119-Gold Nanocage Conjugates to Eradicate Cancer Stem Cells Through a Combination of Photothermal and Chemo Therapies. *Adv. Healthc. Mater.* **3**, 1283–1291 (2014).
72. Hyun, D. C., Levinson, N. S., Jeong, U. & Xia, Y. Emerging Applications of Phase-Change Materials (PCMs): Teaching an Old Dog New Tricks. *Angew. Chemie Int. Ed.* **53**, 3780–3795 (2014).
73. Ayers, F., Grant, A., Kuo, D., Cuccia, D. J. & Durkin, A. J. Fabrication and characterization of silicone-based tissue phantoms with tunable optical properties in the visible and near infrared domain. in *Proceedings of SPIE* (ed. Nordstrom, R. J.) 687007 (SPEI, 2008). doi:10.1117/12.764969
74. Dunklin, J. R. & Roper, D. K. Heat dissipation of resonant absorption in metal nanoparticle-polymer films described at particle separations near resonant wavelength. *J. Nanomater.* **2017**, 2753934 (2017).
75. Howard, T. V., Dunklin, J. R., Forcherio, G. T. & Roper, D. K. Thermoplasmonic dissipation in gold nanoparticle–polyvinylpyrrolidone thin films. *RSC Adv.* **7**, 56463–56470 (2017).

76. Kim, J. *et al.* Engineering structures and functions of mesenchymal stem cells by suspended large-area graphene nanopatterns. *2D Mater.* **3**, 35013 (2016).
77. Wang, Y. *et al.* Fluorinated Graphene for Promoting Neuro-Induction of Stem Cells. *Adv. Mater.* **24**, 4285–4290 (2012).
78. Corning, D. *Sylgard® 184 Silicone Elastomer.* (2014).
79. Yeo, W.-H. *et al.* Multifunctional Epidermal Electronics Printed Directly Onto the Skin. *Adv. Mater.* **25**, 2773–2778 (2013).
80. Jeong, J.-W. *et al.* Wireless Optofluidic Systems for Programmable In Vivo Pharmacology and Optogenetics. *Cell* **162**, 662–674 (2015).
81. McCall, J. G. *et al.* Preparation and implementation of optofluidic neural probes for in vivo wireless pharmacology and optogenetics. *Nat. Protoc.* **12**, 219–237 (2017).
82. Bird, R., Stewart, W. & Lightfoot, E. *Transport Phenomena.* (John Wiley and Sons, Inc., 2007).
83. Mie, G. Contributions to the optics of turbid media, particularly of colloidal metal solutions. *Ann. Phys.* **25**, 377–445 (1908).
84. Dunklin, J. R., Forcherio, G. T. & Roper, D. K. Geometric optics of gold nanoparticle-polydimethylsiloxane thin film systems. *Opt. Mater. Express* **4**, 375–383 (2014).



Size and concentration of resonantly irradiated (green arrows) nanoantennae (gold dots) embedded in soft matter (inside dashed lines) determine the transient rate of thermal dissipation (red arrows) via conduction, convection, and radiation.